Tightly Coupled Integration of BDS-3 B2b RTK, IMU, Odometer, and Dual-Antenna Attitude

Qiaozhuang Xu, Zhouzheng Gao, Jie Lv, and Cheng Yang

***Abstract*—Real Time Kinematic (RTK) based on single-frequency observation is still widely used in many fields due to the characteristics of low-cost and low-power consumption. However, the positioning performance of single-frequency RTK in terms of accuracy, stability, and continuity would be significantly degraded during the harsh satellite environments. To improve the performance, this contribution presented a model of multi-sensor and analytical observations augmented the single frequency RTK tightly based on a modified Psi-angle state model. In such a model, the single frequency observations of the new signal of BDS-3 B2b are tightly integrated with inertial measurements, odometer data, dual-antenna attitude, and non-holonomic constraint. To evaluate the presented model, the typical navigation performance and the ambiguity resolution performance are analyzed based on a set of vehicle-borne data. Results illustrated that the Inertial Navigation System (INS) would bring about 13.5%, 16.2%, and 12.3% position enhancements to the BDS-3 B2b RTK mode. Such improvements could be up to 15.9%, 16.2%, and 25.2% while adding the non-holonomic constraint and odometer data. Besides, non-holonomic constraint and odometer also upgrade the attitude accuracy visibly in pitch and heading directions, with enhancements of about 16.9% and 62.9%. In contrast, augmentations from the dual-antenna attitude are mainly presented in terms of heading angle with about 29.5% compared to the RTK/INS/Odometer/NHC tight integration mode. Besides, the convergence time of yaw angle is visibly enhanced while using the odometer/NHC, the dual-antenna heading, or the two together. Moreover, the ambiguity resolution performance could also be improved while using the presented model. Due to the enhancements in position and attitude brought by different sensors, the ADOP performance would be improved to varying degrees. Besides, the fixed rate and reliability of ambiguity resolution could also be enhanced.**

***Index Terms*—BeiDou Navigation Satellite System (BDS), Single Frequency Real-time Kinematic (SF-RTK), Odometer, Dual-antenna attitude, BDS-3 B2b signal**

This work was partially funded by the National Natural Science Foundation of China (NSFC) (Grants No. 42274022) and the National Key Research and Development Program of China (Grant No. 2020YFB0505802) (Corresponding author: Zhouzheng Gao).

Qiaozhuang Xu is with School of Land Science and Technology, China University of Geosciences (Beijing) (e-mail: qiaozhuangxu@163.com).

Zhouzheng Gao is with School of Land Science and Technology, China University of Geosciences (Beijing) (e-mail: zhouzhenggao@126.com).

Jie Lv is with School of Land Science and Technology, China University of Geosciences (Beijing) (e-mail: lvjiecugb@163.com).

Cheng Yang is with School of Land Science and Technology, China University of Geosciences (Beijing) (e-mail: c.yang@connect.polyu.hk).

I. Introduction

POSITIONING, Navigation, and Timing (PNT) information have become an essential requirement for location-based fields like the Internet of Things (IoT) [1], ocean measurements [2], meteorology [3], and deformation monitoring [4]. Among the current PNT technologies, Global Navigation Satellite System (GNSS), such as BeiDou Navigation Satellite System (BDS), present an excellent space-time sensing capability to provide users with PNT solutions with different grade accuracy. Currently, BDS refers to the second generation BDS (BDS-2) and the third generation BDS (BDS-3) [5], with more than 45 satellites in orbit. In contrast to other systems (i.e., GPS), BDS has stronger anti-jamming capability due to its hybrid orbits of Medium Earth Orbit (MEO), Inclined Geo-Synchronous Orbit (IGSO), and Geostationary Earth Orbit (GEO). In addition, BDS innovatively fuses navigation information with communication information [6]. To meet the requirements of compatibility and interoperability of the inter-GNSS system, BDS-3 adds three new signal frequencies, namely B1C, B2a, and B2b, to the BDS-2 signals of B1I and B3I [7]. As described in [8], B1C has the same frequency (1575.42 MHz) as GPS L1 and Galileo E1. B2a has the same frequency (1176.45 MHz) as GPS L5 and Galileo E5a. B2b has the same frequency (1207.140 MHz) as Galileo E5b. These multi-frequency signals provide significant improvements in the cycle-slip detection [9], ambiguity resolution [10], positioning accuracy and continuity [11], and ionosphere removal [12]. However, the multi-frequency receiver is high cost and high energy consumption. Consequently, there are still a lot of applications based on single-frequency observations.

In recent years, researchers have explored the capability of BDS single-frequency positioning. For example, the observation quality of BDS different signals is analyzed. In [13], a short-baseline experiment was designed to assess the signal quality of B1I and B2I. The result showed that the precision of code and carrier-phase measurements on such two frequencies are comparable to that of GPS. In [14], the multipath effects of BDS-2 GEO satellites were studied. The results showed that the time series of multipath errors vary from 1 m to 2 m. With the completion of BDS-3, scholars also explored the signal quality of BDS-3. In [15], a zero-baseline test with two Trimble Alloy receivers was designed. Results illustrated that the BDS-3 code presents the slightest noise compared to other GNSS systems, and the carrier noise is comparable to these of others. The pseudo-range multipath effects of the three new frequency observations presented in [6] showed that the B2b signal has the most robust anti-multipath ability compared to the worst one of B1C. Meanwhile, the multipath effect of B1I and B3I of BDS-3 was smaller than that of BDS-2. In contrast, more works focused on positioning accuracy. For example, in [16], the positioning performance of GPS, BDS-2, BDS-3, and BDS-2+3 were compared while adopting Precise Point Positioning (PPP) model based on GPS L1, BDS B1I, and BDS B1C. Results showed that horizontal accuracy is better than 0.5 m within 2.5 min at the 68% confidence level except using BDS-2 only mode. In [17], the static Real-time Kinematic (RTK) positioning accuracy of B1I, B3I, B1C, and B2a were investigated under short-baseline conditions. Results showed that millimeter-level positioning could be achieved while using these signals. For the dynamic applications, the positioning accuracy of B1I, B1C, and B2a of BDS-3 adopting single frequency RTK mode were evaluated [18]. Compared to the results of GPS L1 and BDS-2 B1I in the complex observing environments, the RTK of GPS L1 and BDS-3 B1I presented the worst positioning accuracy at about meter-level, and other signals can reach decimeter-level positioning accuracy. Such difference is mainly related to the number of the observation quality, the tracking satellites, and the corresponding Position Dilution of Precision (PDOP).

However, the continuous and high-accuracy positioning results are hard to obtain during harsh GNSS environments. To compensate for the drawback of GNSS, an integration model based on the Extended Kalman Filter (EKF) was presented [19], in which the GPS data and the original Inertial Navigation System (INS) measurements are integrated. In such integration mode, INS provides continuous high-rate results to bridge and smooth GPS solutions. In recent years, some researchers have devoted their research fields to the integration of multi-system and multi-frequency GNSS observations with INS data. For example, a multi-GNSS PPP/INS tight integration model was provided to enhance the reliability, accuracy, and reconvergence time of GNSS PPP [20]. In [21], a GPS/BDS/Galileo PPP-RTK/INS tight integration model was designed and centimeter-level positioning accuracy could be achieved in semi-urban and urban environments. Besides, the ambiguity recovery time was also accelerated with the aid of INS. In [22], a GPS/BDS dual frequencies RTK/INS tight integration model was investigated. Results showed that such a model can significantly improve the ambiguity resolution performance, especially at high cut-off elevations. To reduce the cost and energy consumption in real applications, the integration of GNSS single frequency observations and INS data has also been carried out by some scholars. For example, a real-time sliding estimator for the single frequency RTK/INS tight integration was constructed [23]. Results showed that the position accuracy could achieve decimeter-level. In [24], a multi-GNSS single frequency RTK/INS tight integration model was designed and the positioning performance under short-baseline conditions was analyzed. Results showed that the model could significantly improve the availability and positioning accuracy of RTK in complex environments. To limit the drift speed of INS under GNSS-denied environments, other sensors are used. For example, a single frequency GNSS/INS/Odometer real-time integration system based loosely coupled structure was designed [25]. Results showed that the overall positioning accuracy is 0.31 m, and the power consumption is low. In [26], a GNSS/INS/Visual tight integration model was presented, in which the observations from single-frequency multi-GNSS RTK, IMU, and monocular camera were tightly integrated. Results indicated that the position accuracy could reach centimeter-lever in urban area. Besides, the velocity and attitude could be significantly estimated. In [27], a GNSS/INS/Lidar integration model was provided, and the horizontal positioning error was 0.13 m under the forested environment, which was improved by 70%, compared to that of the GNSS/INS tight integration scheme. In addition, some virtual observations based on the carrier' motion have been considered. As described in [28], the INS measurements, GNSS data, and Non-holonomic Constraint (NHC) could be integrated to reduce the drift of navigation results. Besides, in [29], the contribution of NHC to INS from the observability perspective was investigated. A simulation experiment demonstrated that NHC could improve the observability of attitude and IMU sensor errors. In [30], a mobile phone-based enhanced Pedestrian Dead Reckoning (PDR) model was designed, in which Attitude and Heading Reference System (AHRS) algorithm and zero velocity information in smartphones are utilized to assist RTK. Results showed that the positioning performance in the field of accuracy and continuity could be enhanced using the presented model.

The above works proved that multi-sensor and motion constraints can significantly improve the performance of RTK. To extend the potential application area of BDS-3 RTK/INS system and improve the navigation performance of vehicle-borne under complex urban environments, a tight integration model among BDS-3 B2b RTK, low-cost IMU, odometer, dual-antenna attitude, and analytical constraint is presented in this contribution. Compared to the previous works, the main contributions can be summarized as (1) the odometer and dual-antenna attitude are integrated with single frequency RTK/INS tight integration based on BDS-3 new signal (B2b) and a modified state model, and (2) the Ambiguity Resolution (AR) performance of BDS-3 single frequency RTK could be improved by the enhancements from INS, odometer, and heading data. These contributions make the performance of BDS-3 B2b RTK in terms of positioning accuracy, continuity, and reliability upgrade significantly. The paper is organized as follows. The mathematic models of the odometer, dual-antenna attitude, and analytical constraint tightly aided BDS-3 B2b RTK/INS integration are described in the Methodology part. After that, a set of vehicle-borne data collected around the Beijing's fifth-ring road is analyzed to assess the presented model in terms of typical positioning performance (position, velocity, and attitude) and AR performance. Besides, the influence of the state model on positioning accuracy and ambiguity resolution is also presented. Then, the conclusions are summarized.

II. METHODOLOGY

This section provides a detailed presentation of the proposed methods, including state models, BDS-3 B2b RTK/INS tight integration model, odometer and non-holonomic constraint enhanced model, dual-antenna heading constraint model, and multi-sensor aided ambiguity resolution theory.

A. State models

As described in [20], the state function of the extended Kalman filter for RTK/INS tightly coupled integration can be illustrated as

$$\boldsymbol{X}_k = \boldsymbol{\Phi}_{k,k-1}\boldsymbol{X}_{k,k-1} + \boldsymbol{\eta}_k \tag{1}$$

with

$$\boldsymbol{X}_k = \begin{bmatrix} \delta\boldsymbol{r}_{INS}^n & \delta\boldsymbol{v}_{INS}^n & \boldsymbol{\psi} & \delta\boldsymbol{b}_g & \delta\boldsymbol{b}_a & \delta\boldsymbol{s}_g & \delta\boldsymbol{s}_a & \Delta T_{r,w} & \Delta T_{b,w} & \delta s_o & \nabla\Delta\boldsymbol{N}^T \end{bmatrix}^T \tag{2}$$

where $\boldsymbol{\Phi}_{k,k-1}$ denotes the state transition matrix; $\boldsymbol{X}_k$ represents the state parameter vector; $\boldsymbol{\eta}_k$ is the state noise vector; $\delta\boldsymbol{r}_{INS}^n$, $\delta\boldsymbol{v}_{INS}^n$, and $\boldsymbol{\psi}$ denotes the error vector of position, velocity, and attitude, respectively; $\delta\boldsymbol{b}$ and $\delta\boldsymbol{s}$ are the bias and factor errors of inertial sensors; the subscript g and a represent gyroscope and accelerometer; T is the wet component of the zenith troposphere delay; the subscript b and r represent the base-station and rover-station; δs_o stands for the scale factor error of the odometer; $\nabla\Delta\boldsymbol{N}$ denotes the Double-Differenced (DD) float-ambiguities.

To weak the nonlinear errors of the extended Kalman filter, usually the Psi-angle error model [31] is used

$$\begin{cases} \delta\dot{\boldsymbol{r}}_{INS}^n = -\boldsymbol{\omega}_{en}^n \times \delta\boldsymbol{r}_{INS}^n + \delta\boldsymbol{v}_{INS}^n \\ \delta\dot{\boldsymbol{v}}_{INS}^n = \boldsymbol{f}^n \times \boldsymbol{\psi} + \boldsymbol{C}_b^n\delta\boldsymbol{f}^b - \left(\boldsymbol{\omega}_{ie}^n + \boldsymbol{\omega}_{in}^n\right) \times \delta\boldsymbol{v}_{INS}^n + \delta\boldsymbol{g}^n \\ \dot{\boldsymbol{\psi}} = -\boldsymbol{\omega}_{in}^n \times \boldsymbol{\psi} - \boldsymbol{C}_b^n\delta\boldsymbol{\omega}_{ib}^b \end{cases} \tag{3}$$

where $\boldsymbol{\omega}_{en}^n$ denotes the rotation rate of navigation frame (n-frame) relative to the Earth Centered Earth Fixed frame (e-frame) projected in n-frame; $\boldsymbol{\omega}_{ie}^n$ represents the rotation rate of inertial frame (i-frame) relative to the e-frame projected in n-frame; $\boldsymbol{g}^n$ denotes the gravity vector in n-frame; $\boldsymbol{\omega}_{ib}^b$ and $\boldsymbol{f}^n$ are the gyroscope outputs and accelerometer outputs in b-frame and n-frame; $\boldsymbol{C}_b^n$ is the transition matrix from b-frame to n-frame.

In such a Psi-angle model, the specific force terms may be easily polluted by large biases while using low-cost IMU, which forms an incorrect transition matrix [31]. In [32], a modified Psi-angle model was presented to solve such problem, which can be expressed as

$$\begin{cases} \delta\dot{\boldsymbol{r}}_{INS}^n = -\boldsymbol{\omega}_{en}^n \times \delta\boldsymbol{r}_{INS}^n + \delta\boldsymbol{v}_{INS}^n + \boldsymbol{v}_{INS}^n \times \boldsymbol{\psi} \\ \delta\dot{\boldsymbol{v}}_{INS}^n = \boldsymbol{C}_b^n\delta\boldsymbol{f}^b - \left(\boldsymbol{\omega}_{ie}^n + \boldsymbol{\omega}_{in}^n\right) \times \delta\boldsymbol{v}_{INS}^n + \delta\boldsymbol{g}^n - \boldsymbol{g}^n \times \boldsymbol{\psi} - \boldsymbol{v}_{INS}^n \times \left(\boldsymbol{\omega}_{ie}^n \times \boldsymbol{\psi}\right) + \boldsymbol{v}_{INS}^n \times \boldsymbol{C}_b^n\delta\boldsymbol{\omega}_{ib}^b \\ \dot{\boldsymbol{\psi}} = -\boldsymbol{\omega}_{in}^n \times \boldsymbol{\psi} - \boldsymbol{C}_b^n\delta\boldsymbol{\omega}_{ib}^b \end{cases} \tag{4}$$

where $\boldsymbol{\omega}_{in}^n$ denotes the angle rate of n-frame relative to the i-frame projected in n-frame;

To limit IMU drift over time, the IMU sensors' errors are usually augmented to the state vector and modeled as First-order Gauss-Markov processes [31].

$$\begin{pmatrix} \delta\dot{\boldsymbol{b}}_g \\ \delta\dot{\boldsymbol{b}}_a \\ \delta\dot{\boldsymbol{s}}_g \\ \delta\dot{\boldsymbol{s}}_a \end{pmatrix} = \begin{pmatrix} -\frac{1}{\tau_{b_g}}\delta\boldsymbol{b}_g \\ -\frac{1}{\tau_{b_a}}\delta\boldsymbol{b}_a \\ -\frac{1}{\tau_{s_g}}\delta\boldsymbol{s}_g \\ -\frac{1}{\tau_{s_a}}\delta\boldsymbol{s}_a \end{pmatrix} + \boldsymbol{w} \tag{5}$$

where τ is the correlation time of the process; $\boldsymbol{w}$ is the driving white noise.

Besides, the gyroscope noises and accelerometer noises are processed as Angle Random Walk (ARW) and Velocity Random Walk (VRW), respectively. Besides, the odometer scale factor and zenith troposphere delay parameters can also be modeled as a random walk process. The DD float-ambiguities can be processed as Random Constant [33]. Such two stochastic models can be expressed as

$$\begin{cases} \dot{x}_k = \omega_{k-1} \\ \dot{x}_k = 0 \end{cases} \tag{6}$$

where the symbols are the same as these mentioned above.

Based on the state models in Eqs. (4) ~ (6), the transition matrix can be achieved by applying a digital integration

$$\boldsymbol{\Phi}_{k,k-1} = \begin{bmatrix} \boldsymbol{\Phi}_{r,r} & \boldsymbol{\Phi}_{r,v} & \boldsymbol{\Phi}_{r,\psi} & \boldsymbol{0} & \boldsymbol{0} & \boldsymbol{0} & \boldsymbol{0} & 0 & 0 & 0 & \boldsymbol{0} \\ \boldsymbol{\Phi}_{v,r} & \boldsymbol{\Phi}_{v,v} & \boldsymbol{\Phi}_{v,\psi} & \boldsymbol{\Phi}_{v,b_g} & \boldsymbol{\Phi}_{v,b_a} & \boldsymbol{\Phi}_{v,s_g} & \boldsymbol{\Phi}_{v,s_a} & 0 & 0 & 0 & \boldsymbol{0} \\ \boldsymbol{0} & \boldsymbol{0} & \boldsymbol{\Phi}_{\psi,\psi} & \boldsymbol{\Phi}_{\psi,b_g} & \boldsymbol{0} & \boldsymbol{\Phi}_{\psi,s_g} & \boldsymbol{0} & 0 & 0 & 0 & \boldsymbol{0} \\ \boldsymbol{0} & \boldsymbol{0} & \boldsymbol{0} & \boldsymbol{\Phi}_{b_g,b_g} & \boldsymbol{0} & \boldsymbol{0} & \boldsymbol{0} & 0 & 0 & 0 & \boldsymbol{0} \\ \boldsymbol{0} & \boldsymbol{0} & \boldsymbol{0} & \boldsymbol{0} & \boldsymbol{\Phi}_{b_a,b_a} & \boldsymbol{0} & \boldsymbol{0} & 0 & 0 & 0 & \boldsymbol{0} \\ \boldsymbol{0} & \boldsymbol{0} & \boldsymbol{0} & \boldsymbol{0} & \boldsymbol{0} & \boldsymbol{\Phi}_{s_g,s_g} & \boldsymbol{0} & 0 & 0 & 0 & \boldsymbol{0} \\ \boldsymbol{0} & \boldsymbol{0} & \boldsymbol{0} & \boldsymbol{0} & \boldsymbol{0} & \boldsymbol{0} & \boldsymbol{\Phi}_{s_a,s_a} & 0 & 0 & 0 & \boldsymbol{0} \\ \boldsymbol{0} & \boldsymbol{0} & \boldsymbol{0} & \boldsymbol{0} & \boldsymbol{0} & \boldsymbol{0} & \boldsymbol{0} & 1 & 0 & 0 & \boldsymbol{0} \\ \boldsymbol{0} & \boldsymbol{0} & \boldsymbol{0} & \boldsymbol{0} & \boldsymbol{0} & \boldsymbol{0} & \boldsymbol{0} & 0 & 1 & 0 & \boldsymbol{0} \\ \boldsymbol{0} & \boldsymbol{0} & \boldsymbol{0} & \boldsymbol{0} & \boldsymbol{0} & \boldsymbol{0} & \boldsymbol{0} & 0 & 0 & 1 & \boldsymbol{0} \\ \boldsymbol{0} & \boldsymbol{0} & \boldsymbol{0} & \boldsymbol{0} & \boldsymbol{0} & \boldsymbol{0} & \boldsymbol{0} & 0 & 0 & 0 & I_{q\times q} \end{bmatrix} \tag{7}$$

with

$$\begin{cases} \boldsymbol{\Phi}_{r,r} = \left[I - \left(\boldsymbol{\omega}_{en}^n \times\right)\Delta t\right]_{3\times3}, \boldsymbol{\Phi}_{r,v} = \left[I\Delta t\right]_{3\times3}, \boldsymbol{\Phi}_{r\psi} = \left[\left(\boldsymbol{v}_{INS}^n \times\right)\Delta t\right]_{3\times3} \\ \boldsymbol{\Phi}_{v,r} = -g\Delta t diag((R_M+h)^{-1}, (R_M+h)^{-1}, 2(\sqrt{R_N R_M}+h)^{-1}) \\ \boldsymbol{\Phi}_{v,v} = \left[I - \left(\left(\boldsymbol{\omega}_{ie}^n + \boldsymbol{\omega}_{in}^n\right)\Delta t\right)\times\right]_{3\times3} \\ \boldsymbol{\Phi}_{v,b_g} = \left[\left(\boldsymbol{v}_{INS}^n \times \boldsymbol{C}_b^n\right)\Delta t\right]_{3\times3}, \boldsymbol{\Phi}_{v,b_a} = \left(\boldsymbol{C}_b^n\Delta t\right)_{3\times3}, \boldsymbol{\Phi}_{v,s_g} = \left[\left(\boldsymbol{v}_{INS}^n \times \boldsymbol{C}_b^n\right)\boldsymbol{\omega}_{ib}^b\Delta t\right]_{3\times3} \\ \boldsymbol{\Phi}_{v,s_a} = \left(\boldsymbol{C}_b^n\boldsymbol{f}^b\Delta t\right)_{3\times3}, \ \boldsymbol{\Phi}_{\psi,\psi} = \left[I - \left(\boldsymbol{\omega}_{in}^n \times\right)\Delta t\right]_{3\times3}, \boldsymbol{\Phi}_{\psi,b_g} = -\left(\boldsymbol{C}_b^n\Delta t\right)_{3\times3} \\ \boldsymbol{\Phi}_{\psi,s_g} = -\left(\boldsymbol{C}_b^n\boldsymbol{\omega}_{ib}^b\Delta t\right)_{3\times3}, \ \boldsymbol{\Phi}_{b_g,b_g} = \left[Ie^{-\Delta t/\tau_{b_g}}\right]_{3\times3}, \ \boldsymbol{\Phi}_{b_a,b_a} = \left[Ie^{-\Delta t/\tau_{b_a}}\right]_{3\times3} \\ \boldsymbol{\Phi}_{s_g,s_g} = \left[Ie^{-\Delta t/\tau_{s_g}}\right]_{3\times3}, \ \boldsymbol{\Phi}_{s_a,s_a} = \left[Ie^{-\Delta t/\tau_{s_a}}\right]_{3\times3} \\ \boldsymbol{\Phi}_{v,\psi} = \begin{bmatrix} v_D\omega_e sin\psi & -g + v_E\omega_e cos\psi & v_D\omega_e cos\psi \\ g & v_D\omega_e sin\psi - v_N\omega_e cos\psi & 0 \\ -v_N\omega_e sin\psi & -v_E\omega_e sin\psi & -v_N\omega_e cos\psi \end{bmatrix}\Delta t \end{cases} \tag{8}$$

where Δt denotes the sampling rates of IMU, the other symbols are the same as these mentioned above.

B. Observation models

In this subsection, the models for integrating the INS-updated information (position, velocity, and attitude) with B2b observations (pseudo-range and carrier-phase), odometer data, dual-antenna attitude, and non-holonomic pseudo-observations are provided.

1) BDS-3 B2b RTK/INS tight integration

The core idea of B2b RTK/INS tight integration is to fuse the INS-predicted position and B2b observations. According to [24], the measurement function of the RTK/INS tight integration can be illustrated as

$$\boldsymbol{Z}_{BDS,k} = \boldsymbol{H}_{BDS,k}\boldsymbol{X}_k + \boldsymbol{V}_{BDS,k} \tag{9}$$

with

$$\boldsymbol{Z}_{BDS,k} = \begin{bmatrix} \nabla\Delta\hat{\boldsymbol{\rho}}_{INS} \\ \nabla\Delta\hat{\boldsymbol{\rho}}_{INS} \end{bmatrix} - \begin{bmatrix} \nabla\Delta P_{BDS} \\ \lambda\left(\nabla\Delta\varphi_{BDS} + \nabla\Delta N_{BDS}\right) \end{bmatrix} + \begin{bmatrix} \Delta R_T \\ \Delta R_T \end{bmatrix} + \begin{bmatrix} p_{l,IB} \\ p_{l,IB} \end{bmatrix} \tag{10}$$

where $\boldsymbol{H}_{BDS,k}$ denotes the designed coefficient matrix; $\boldsymbol{V}_{BDS,k}$ is the residual vector; $\hat{\boldsymbol{\rho}}_{INS}$ denotes the INS-predicted distance between the antenna centers of satellite and receiver; P_{BDS} and φ_{BDS} represent the pseudo-range and carrier-phase; $R_T = \Delta F_r \Delta T_{r,w} - \Delta F_b \Delta T_{b,w}$, wherein R_T represents the inter-station wet troposphere delay in slant direction [18], F is the projection function of the troposphere delay; $p_{l,IB}$ denotes the distance form of lever-arm offset between the centers of IMU and BDS receiver antenna [33].

By applying the Taylor series expansion on Eq. (10) around Eq. (2), and considering the lever-arm offset and the transformation between *n*-frame and *e*-frame, the designed coefficient matrix can be written as

$$\boldsymbol{H}_{BDS,k} = \begin{bmatrix} \boldsymbol{A}\cdot\boldsymbol{C}_1 & \boldsymbol{0}_{q\times3} & \boldsymbol{A}\cdot\boldsymbol{C}_1\cdot\boldsymbol{C}_2 & \boldsymbol{0}_{q\times12} & \Delta F_r & -\Delta F_b & \boldsymbol{0}_{q\times q} \\ \boldsymbol{A}\cdot\boldsymbol{C}_1 & \boldsymbol{0}_{q\times3} & \boldsymbol{A}\cdot\boldsymbol{C}_1\cdot\boldsymbol{C}_2 & \boldsymbol{0}_{q\times12} & \Delta F_r & -\Delta F_b & \boldsymbol{\lambda}_{q\times q} \end{bmatrix} \tag{11}$$

where $\boldsymbol{\lambda}$ is the carrier wavelength; $\boldsymbol{A}$ denotes the designed matrix containing the DD receiver-satellite direction vector; the subscript m denotes the BDS-3 satellite numbers; $\boldsymbol{C}_2 = \left[\left(\boldsymbol{C}_b^n\boldsymbol{l}_{BDS}^b\right)\times\right]$, and $\boldsymbol{l}_{BDS}^b$ is the lever-arm vector from centers of IMU and BDS receiver antenna in *b*-frame; $\boldsymbol{C}_1$ denotes the transition matrix from *e*-frame to the *n*-frame, which can be expressed as

$$\boldsymbol{C}_1 = \begin{bmatrix} \dfrac{-\left(R_N+h\right)cos\,\gamma\,sinB}{R_M+h} & -sin\,\gamma & -cos\,B\,cos\,\gamma \\ \dfrac{-\left(R_N+h\right)sin\,B\,sin\,\gamma}{R_M+h} & cos\,\gamma & -cos\,B\,sin\,\gamma \\ \dfrac{\left[R_N\left(1-e^2\right)+h\right]cos\,B\,sin\,\gamma}{R_M+h} & 0 & -sin\,B \end{bmatrix} \tag{12}$$

where B, γ, and h represent geodetic latitude, longitude, and height; R_N and R_M denote the radius of curvature in prime vertical and meridian; e is earth eccentricity.

2) Odometer and NHC enhanced B2b RTK/INS tight integration

A vehicle-borne carrier should keep in touch with the ground, which means that only velocity in the forward direction exists, and the velocities in the lateral and vertical directions should be close to zero when there are no slip and jump. It provides two pseudo velocity observations in the motor-vehicle frame (m-frame)

$$\boldsymbol{v}_{NHC}^m \approx \begin{bmatrix} 0 & 0 \end{bmatrix}^{\mathrm{T}} \tag{13}$$

The velocity in forward direction can be measured by an odometer. Then a three-dimension holonomic constraint is formed

$$\boldsymbol{v}_o^m \approx \begin{bmatrix} \dfrac{v_F^m}{1+s_o} & \boldsymbol{v}_{NHC}^m \end{bmatrix}^{\mathrm{T}} \approx \begin{bmatrix} \dfrac{v_F^m}{1+s_o} & 0 & 0 \end{bmatrix}^{\mathrm{T}} \tag{14}$$

where v_F^m is the forward velocity measured by the odometer; s_o denotes the scale error of the odometer.

The measurement function can be written as

$$Z_o = v_o^m - \boldsymbol{C}_b^m\left(\boldsymbol{C}_n^b\boldsymbol{v}_{INS}^n + \boldsymbol{\omega}_{ib}^b \times \boldsymbol{l}_o^b\right) \tag{15}$$

with the error disturbance expression of

$$\delta Z_o = v_o^m s_o - C_b^m\left(C_n^b\delta v_{INS}^n - C_n^b\left(v_{INS}^n\times\right)\psi - \left(l_o^b\times\right)\delta b_g - \left(l_o^b\times\right)\omega_{ib}^b\delta s_g\right) \tag{16}$$

where l_o^b denotes the lever-arm from the IMU center to the odometer center in the *b*-frame.

The corresponding designed matrix can be expressed as

$$\boldsymbol{H}_{o,k} = \begin{bmatrix} \boldsymbol{0}_{3\times3} & -\boldsymbol{C}_b^m\boldsymbol{C}_n^b & \boldsymbol{C}_b^m\boldsymbol{C}_n^b\left(\boldsymbol{v}_{INS}^n\times\right) & \boldsymbol{C}_b^m\left(\boldsymbol{l}_o^b\times\right) & \boldsymbol{C}_b^m\left(\boldsymbol{l}_o^b\times\right)\boldsymbol{\omega}_{ib}^b & 0 & 0 & \boldsymbol{v}_o^m & \boldsymbol{0}_{3\times q} \end{bmatrix} \tag{17}$$

where the symbols are the same as these mentioned above.

3) Dual-antenna attitude enhanced B2b RTK/INS tight integration

As mentioned in [34, 35], the estimation accuracy of the heading angle is much lower than roll and pitch due to the weak observability of the gyroscope in the vertical direction. To improve heading angle accuracy, the heading angle provided by dual-antenna BDS-3 is introduced in our work.

According to [35], the baseline vector in *n*-frame can be represented by

$$\left(x^n, \mathrm{y}^n, z^n\right)^T = \boldsymbol{C}_u^n\left(x^u, \mathrm{y}^u, z^u\right)^T \tag{18}$$

where $\left(x^u, \mathrm{y}^u, z^u\right)$ denotes the baseline vector in GNSS-antenna frame; $\boldsymbol{C}_u^n$ denotes the transition matrix from GNSS-antenna-frame to the *n*-frame.

Then, the heading angle provided by dual-antenna can be obtained by

$$\hat{\theta} = atan2\left(\mathrm{y}^n, x^n\right) \tag{19}$$

where $atan2\left(\cdot\right)$ denotes the inverse tangent function.

According to [31], the heading pseudo observation function can be expressed by

$$Z_{Heading,k} = \theta - \hat{\theta} \tag{20}$$

$$\delta Z_{Heading,k} = H_{heading,k}\psi \tag{21}$$

$$H_{heading,k} = \begin{bmatrix} \dfrac{\sum_{i=1}^{3}\left(C'_{3i}C''_{i1}\right)\left(C_v^n\right)_{11}}{\left(C_v^n\right)_{11}^2+\left(C_v^n\right)_{21}^2} \\ \dfrac{\sum_{i=1}^{3}\left(C'_{3i}C''_{i1}\right)\left(C_v^n\right)_{21}}{\left(C_v^n\right)_{11}^2+\left(C_v^n\right)_{21}^2} \\ -\dfrac{\sum_{i=1}^{3}\left(C'_{1i}C''_{i1}\right)\left(C_v^n\right)_{11}+\sum_{i=1}^{3}\left(C'_{2i}C''_{i1}\right)\left(C_v^n\right)_{21}}{\left(C_v^n\right)_{11}^2+\left(C_v^n\right)_{21}^2} \end{bmatrix} \tag{22}$$

where θ and $\hat{\theta}$ denote the heading angles from the INS-updated solutions and the dual-antenna BDS-3 solutions, respectively; C' denotes the direction cosine matrix for the transformation from *b*-frame to *n*-frame; C'' is derived from C_v^b; the subscripts i and j ($1 \le i, j \le 3$) are the i th line and j th column element.

C. Multi-sensor augmented ambiguity resolution

As common sense, correct and reliable ambiguity resolution is the key for the carrier-phase based high-accuracy positioning. However, the AR performance based on single frequency is generally worse due to the frequent signal outages and low-accuracy observations, especially in a constrained and dynamic environment [36]. Fortunately, recent researchers showed that adding other sensors like INS could improve float ambiguity estimation and compress the ambiguity search space [24, 37]. To furtherly illustrate the superiority of the presented model, the theory of multi-sensor augmented ambiguity resolution will be introduced in this part.

To be more simplicity, the state vector can be re-expressed as

$$\boldsymbol{X}_k = \left[\boldsymbol{X}_{\hat{s}} \quad \boldsymbol{X}_{\hat{o}} \quad \boldsymbol{X}_{\hat{a}}\right]^T \tag{23}$$

with

$$\boldsymbol{X}_s = \left[\delta \boldsymbol{r}_{INS}^n \quad \psi \quad \boldsymbol{X}_2\right]^T \tag{24}$$

where $\boldsymbol{X}_2$ denotes the state vector related to the velocity error, IMU sensor error, and residual zenith wet delay errors; $\boldsymbol{X}_{\hat{o}}$ represents the scale factor error of the odometer; $\boldsymbol{X}_{\hat{a}}$ is the DD ambiguities vector.

The prior state covariance predicted by Extended Kalman Filter (EKF) can be expressed as

$$\boldsymbol{P}^- = \begin{bmatrix} \boldsymbol{P}_{\hat{s}} & \boldsymbol{P}_{\hat{s}\hat{o}} & \boldsymbol{P}_{\hat{s}\hat{a}} \\ \boldsymbol{P}_{\hat{s}\hat{o}}^T & \boldsymbol{P}_{\hat{o}} & \boldsymbol{P}_{\hat{o}\hat{a}} \\ \boldsymbol{P}_{\hat{s}\hat{a}}^T & \boldsymbol{P}_{\hat{o}\hat{a}}^T & \boldsymbol{P}_{\hat{a}} \end{bmatrix}, \boldsymbol{P}_{\hat{s}} = \begin{bmatrix} \boldsymbol{P}_{\delta r} & \boldsymbol{P}_{\delta r\psi} & \boldsymbol{P}_{\delta r2} \\ \boldsymbol{P}_{\delta r\psi}^T & \boldsymbol{P}_{\psi} & \boldsymbol{P}_{\psi 2} \\ \boldsymbol{P}_{\delta r2}^T & \boldsymbol{P}_{\psi 2}^T & \boldsymbol{P}_2 \end{bmatrix} \tag{25}$$

where the subscripts are the same as these in Eqs. (23) and (24).

Assuming that there are complete satellite outages at the last epoch, the simplified covariances of ambiguity can be written as

$$\begin{cases} \boldsymbol{P}_{\hat{a}} = \sigma_0^2 \\ \boldsymbol{P}_{\hat{s}\hat{a}} = 0 \\ \boldsymbol{P}_{\hat{o}\hat{a}} = 0 \end{cases} \tag{26}$$

where σ_0^2 denotes the re-initialized covariance of float ambiguity. By applying Eqs.(10), (15), and (20), the measurement function can be summarized as

$$\boldsymbol{V}_z = \underbrace{\begin{bmatrix} \boldsymbol{H}_{\hat{s}} & 0 & 0 \\ \boldsymbol{H}_{\hat{s}\hat{o}} & \boldsymbol{v}_{od} & 0 \\ \boldsymbol{H}_{\hat{s}} & 0 & \boldsymbol{H}_{\hat{a}} \\ \boldsymbol{H}_{\hat{s}\hat{\psi}} & 0 & 0 \end{bmatrix}}_{\boldsymbol{H}} \begin{bmatrix} \boldsymbol{X}_s \\ \boldsymbol{X}_o \\ \boldsymbol{X}_a \end{bmatrix} + \boldsymbol{\eta}_z \tag{27}$$

where $\boldsymbol{V}_z$ is the measurement error vector; $\boldsymbol{H}_{\hat{a}} = \left[\lambda \boldsymbol{I}_{q\times q}\right]$ denotes the design matrix of float ambiguities; $\boldsymbol{H}_{\hat{s}}$, $\boldsymbol{H}_{\hat{s}\hat{o}}$, and $\boldsymbol{H}_{\hat{s}\hat{\psi}}$ represent the matrices of the position error, velocity error, attitude error, IMU sensor error, and residual zenith wet delay errors, which can be found in Eqs. (11), (17), and (22); $\boldsymbol{\eta}_z$ is the measurement noise vector, with the covariance matrix of

$$\boldsymbol{R} = \begin{bmatrix} \boldsymbol{R}_p & 0 & 0 & 0 \\ 0 & \boldsymbol{R}_o & 0 & 0 \\ 0 & 0 & \boldsymbol{R}_{\varphi} & 0 \\ 0 & 0 & 0 & \boldsymbol{R}_{\theta} \end{bmatrix} \tag{28}$$

where $\boldsymbol{R}_p$, $\boldsymbol{R}_o$, $\boldsymbol{R}_{\varphi}$ and $\boldsymbol{R}_{\theta}$ stand for the prior variance of pseudo-range, odometer, carrier-phase, and heading angle, respectively;

According to [38], the posterior state covariance can be applied

$$\boldsymbol{P}^+ = \boldsymbol{P}^- - \boldsymbol{P}^-\boldsymbol{H}^T\left(\boldsymbol{H}\boldsymbol{P}^-\boldsymbol{H}^T + \boldsymbol{R}\right)^{-1}\boldsymbol{H}\boldsymbol{P}^- \tag{29}$$

where the symbols are the same as the above. Substituting Eqs. (25), (26), (27), and (28) into Eq. (29), the posterior state covariance of the updated float ambiguities can be expressed as

$$\boldsymbol{P}_{\hat{a}}^+ = \boldsymbol{P}_{\hat{a}}^- - \lambda^2\boldsymbol{P}_{\hat{a}}^-\begin{pmatrix} \boldsymbol{A}\boldsymbol{C}_1\boldsymbol{P}_{\sigma r}^-\boldsymbol{C}_1^T\boldsymbol{A}^T + \boldsymbol{A}\boldsymbol{C}_1\boldsymbol{C}_2\boldsymbol{P}_{\sigma\psi r}^-\boldsymbol{C}_1^T\boldsymbol{A}^T + \boldsymbol{A}\boldsymbol{C}_1\boldsymbol{P}_{\sigma r\psi}^-\boldsymbol{C}_2^T\boldsymbol{C}_1^T\boldsymbol{A}^T \\ +\boldsymbol{A}\boldsymbol{C}_1\boldsymbol{C}_2\boldsymbol{P}_{\psi}^-\boldsymbol{C}_2^T\boldsymbol{C}_1^T\boldsymbol{A}^T + \lambda^2\boldsymbol{P}_{\hat{a}}^- + \boldsymbol{R}_{\varphi} \end{pmatrix}^{-1}\boldsymbol{P}_{\hat{a}}^- \tag{30}$$

where $\boldsymbol{P}_{\hat{a}}^-$ denotes the prior state covariance of float ambiguities.

According to Eq. (30), it can be concluded that $\boldsymbol{P}_{\hat{a}}^+$ is only influenced by the satellite geometry $\boldsymbol{A}$ and the prior poses information ($\boldsymbol{P}_{pose}^- = \left(\boldsymbol{P}_{\sigma r}^-, \boldsymbol{P}_{\sigma r\psi}^-, \boldsymbol{P}_{\psi}^-\right)$). Assuming that there are two prior poses information, a matrix inequality can be expressed as

$$\boldsymbol{P}_{\hat{a},1}^+ < \boldsymbol{P}_{\hat{a},2}^+, \text{if } \boldsymbol{P}_{pose,1}^- < \boldsymbol{P}_{pose,2}^- \tag{31}$$

if the accuracy of the prior poses is high, the float ambiguity will be better estimated. According to [39], the Ambiguity Dilution of Precision (ADOP) is a scalar diagnostic to measure the volume of the ambiguity search space and the intrinsic model strength of the successful ambiguity resolution, which is defined as

$$ADOP=\sqrt[n]{\left|\boldsymbol{P}_{\hat{a}}^{+}\right|} \tag{32}$$

where n denotes the dimension of the ambiguity vector. Considering Eq. (31), Eq. (32) implies $ADOP_1 < ADOP_2$, if $\boldsymbol{P}_{pose,1}^{-} < \boldsymbol{P}_{pose,2}^{-}$. Therefore, it can be concluded that more accurate poses information provides higher ambiguities fixing rate.

D. Algorithm summary

Based on the models presented above, the algorithm can be described by Fig. 1. According to the time synchronization results among IMU measurements, BDS-3 observations, odometer velocity, and dual-antenna-based heading measurements, the integration schemes of the RTK/INS tight integration mode, the INS only mode, INS/odometer integration mode, odometer and INS tightly aided RTK mode, and heading measurements tightly aided RTK/INS/odometer mode, respectively can be adopted. In the initialization phase, the dual-antenna BDS-3 RTK provides the initial position, velocity, and heading attitude. Then, these information as well as IMU raw data are adopted to provide the initial information for the Kalman filter. Then, the compensated IMU data are used by INS mechanization to provide the INS-predicted position, velocity, and attitude. After the time update phase of the Kalman filter, the measurement update of the Kalman filter will work and the corresponding innovation vector would be generated according to the availabilities of BDS-3 observations, odometer measurements, and heading measurements at current epoch. When BDS-3 data is available, the LAMBDA method is utilized for ambiguity resolution and the "continuous" ambiguity fixing strategy [40] is adopted for ambiguity inheriting. In this phase, the ratio-test and model-driven bootstrapped success rate test will be used to confirm the correctness of the fixed ambiguities. If the searched ambiguities pass the validation test, the selected mode can be obtained by only using the high-precision carrier phase measurements. Otherwise, the float solutions are feedback.

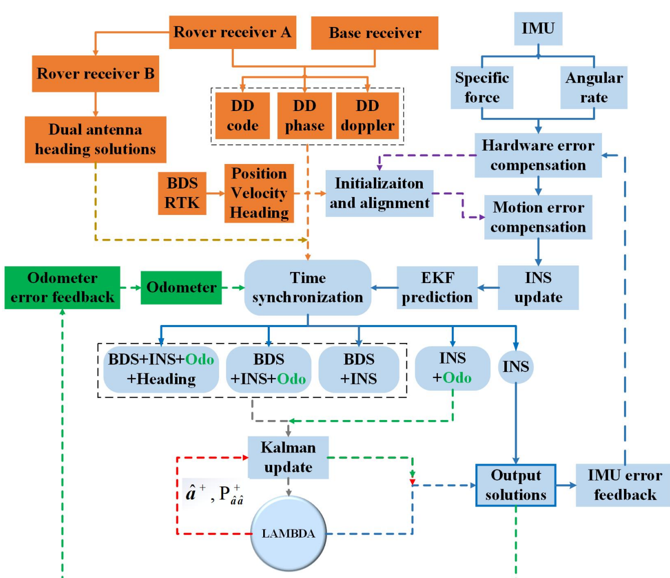

Fig. 1. Implementation of the multi-sensor and analytical constraints augmented the BDS-3 RTK model.

III. Experiments, Evaluations, and Discussions

To evaluate the comprehensive performance of the presented method in a classic urban environment, a set of two-hour vehicle-borne data collected in Beijing, China, on December 12, 2021, was processed and analyzed. During this test, dual-antenna multi-constellation GNSS receivers, a MEMS-grade IMU, and an odometer sensor were rigidly fixed on a vehicle to obtain the 1 Hz BDS-3 observations, 200 Hz IMU measurements, 1 Hz odometer data, and the 1 Hz dual-antenna heading observations was. The main specifications of the IMU can be found in Table I, which indicates it is a low-grade MEMS IMU. The trajectory of this test, as plotted in the top subfigure of Fig. 2, is about 26.0 km in the west-east direction and about 39.0 km along the north-south direction, which is located along the fifth ring road in Beijing. In the test, the vehicle velocities are within ±35m/s, as shown in the bottom subfigure of Fig. 2.

TABLE I

PERFORMANCE SPECIFICATIONS OF THE IMU SENSORS

Bias		Random Walk	
Gyro. ($°/h$)	Acce. (mGal)	Angular ($°/\sqrt{h}$)	Velocity ($m/s/\sqrt{h}$)
36	3000	3.17	2.7

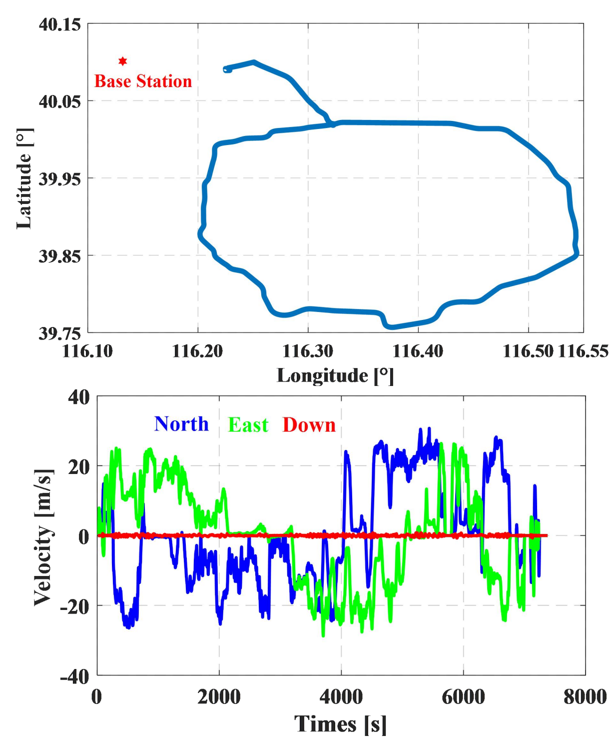

Fig. 2. Trajectory (top) and velocity (bottom) of the vehicle experiment

To make the investigation clear, the solutions based on both single-frequency observations of BDS-3 B1I and BDS-3 B2b were presented. In general, these measured data were analyzed by the schemes of (1) BDS-3 B1I RTK (B1I-R), (2) BDS-3 B2b RTK (B2b-R), (3) BDS-3 B1I RTK/INS tightly coupled integration (B1I-RI), (4) BDS-3 B2b RTK/INS (B2b-RI) tightly coupled integration, (5) BDS-3 B1I RTK/INS tightly coupled integration based on the Psi-angle state model (B1I-PRI), (6) BDS-3 B2b RTK/INS based on the Psi-angle state model (B2b-PRI), (7) BDS-3 B1I RTK/INS/Odometer tightly coupled integration (B1I-RIO), (8) BDS-3 B2b RTK/INS/Odometer tightly coupled integration (B2b-RIO), (9) BDS-3 B1I RTK/INS/Odometer/Heading tightly coupled integration (B1I-RIOH), (10) BDS-3 B2b RTK/INS/Odometer/Heading (B2b-RIOH), respectively. The specific differences of these schemes are listed in Table II. For ambiguity procession, the ratio-test and success-rate were set to 3.00 and 0.99 [41]. In the validation, the above schemes are compared to the reference values provided by the Rauch–Tung–Striebel (RTS)-smoothed dual-frequency GPS+BDS RTK/INS tight integration from Inertial Explorer software. During the analysis part, the improvements in the performance of Positioning, Velocimetry, and Attitude determination (PVA) from our methods are presented in detail.

TABLE II
SPECIFIC DIFFERENCES BETWEEN DIFFERENT SCHEMES

Schemes	B2b data	B1I data	IMU	Odo	Heading	Psi	M-psi
B1I-R	×	√	×	×	×	×	×
B2b-R	√	×	×	×	×	×	×
B1I-RI	×	√	√	×	×	√	×
B2b-RI	√	×	√	×	×	√	×
B1I-PRI	×	√	√	×	×	×	√
B2b-PRI	√	×	√	×	×	×	√
B1I-RIO	×	√	√	√	×	×	√
B2b-RIO	√	×	√	√	×	×	√
B1I-RIOH	×	√	√	√	√	×	√
B2b-RIOH	√	×	√	√	√	×	√

A. Quality of single-frequency observations

In general, observations with low quality would significantly impact the positioning performance of these satellite-based navigation technologies. Consequently, the qualities of BDS-3 observation in terms of available satellite number, PDOP, the ratio of the Signal to Noise Ratio (SNR), and multipath noise were analyzed in this subsection.

1) Satellite availability

As shown in Fig. 3, only MEO satellites were tracked during the test. The availability of satellites and the corresponding PDOP indicate that there are frequent partial and complete satellite signal outages during the test. The number of a such signal-outage phenomena amounts to 453. Since the performance of RTK is highly related to the continuity of carrier phase, it could be a prognosis that its positioning accuracy would be rather low because of the frequent re-convergence or re-initialization caused by the signal outages. According to the statistics, the satellites number of B2b and B1I on average are 7.1 and 7.2, and the corresponding PDOP are 3.0 and 3.5.

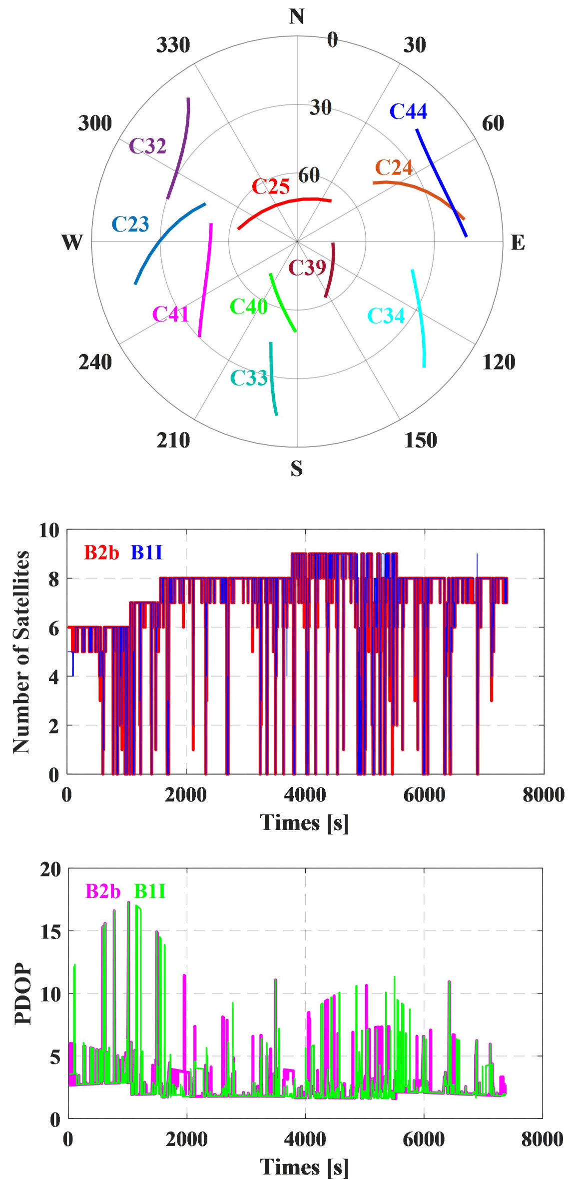

Fig. 3. Sky-plot of the observed BDS-3 satellites (top), available number of satellites (middle) and the corresponding PDOP (bottom) of BDS-3 B2b and B1I in the vehicle test.

2) SNR and multipath

Besides available satellites, the observation qualities in terms of SNR and multipath noise are also essential indexes for RTK positioning. The information of SNR and multipath during this test are provided in Figs. 4 and 5. Accordingly, the SNR values of B1I and B2b signals range from 30 dB to 55 dB, with values on average of 48.64 dB and 47.28 dB. The corresponding Root-Mean-Square (RMS) values are about 48.70 dB and 47.38 dB. About 81.32% B2b signals and 93.84% B1I signals are more than 45 dB on average. Compared to [15], the signal tracking strength in this test is supposed to be strong. We also noticed that the SNR of C44 is lower than that of the other satellites. This is because of the lower-evaluation angle, as plotted in the top subfigure in Fig. 3. Besides, the multipath in this test is visible. According to the plots, the multipath strength of B1I and B2b within ±2 m, which is close to the solutions in [15]. Similar to SNR, the observation quality on B1I is higher than those on B2b. Meanwhile, it also can be found that the SNR and multipath are strongly related to the available satellites.

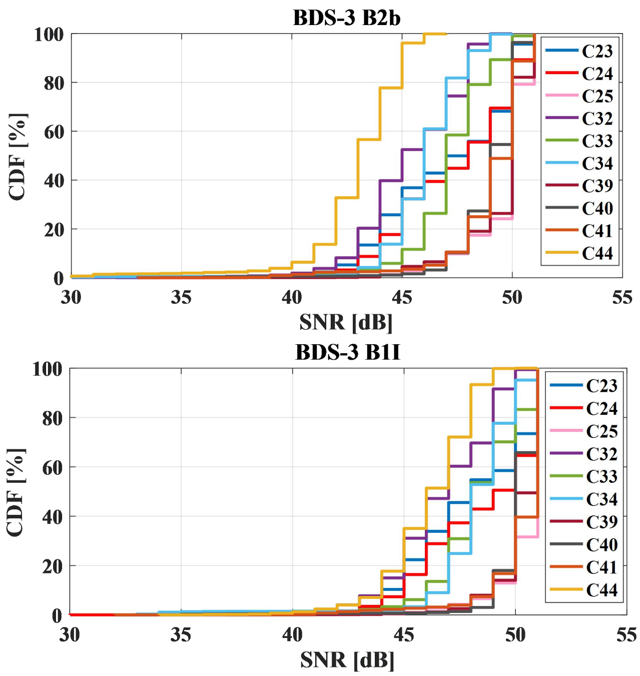

Fig. 4. The Cumulative Distribution Functions (CDF) of signal/noise ratio of BDS-3 B2b (top) and BDS-3 B1I (bottom).

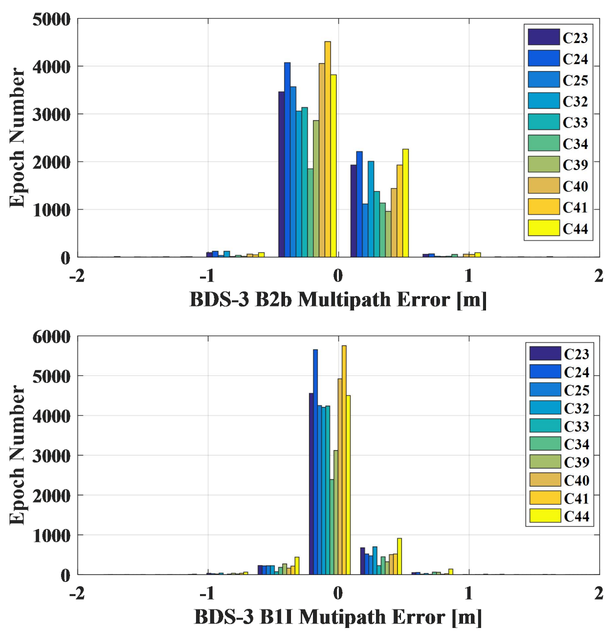

Fig. 5. The histograms of pseudorange multipath of BDS-3 B2b (top) and BDS-3 B1I (bottom).

B. Enhancements on vehicle-borne single-frequency PVA

The performance of the presented method in terms of position accuracy, velocity accuracy, and attitude accuracy are presented in this part.

1) Impacts on positioning

Shown in Fig. 6 are the position differences of B2b-based modes by comparing with the reference values, and the corresponding RMSE results are listed in Tables III. It can be seen that the positioning performance of RTK-only mode could be reached decimeter-level at the majority of epochs, which satisfy the conclusions in [18]. However, there are still many epochs with positioning errors bigger than one meter. Comparing to the observability of BDS-3 satellites in Fig. 3, it can be concluded that such accuracy degradation epochs are strongly related to the weak satellite availability periods.

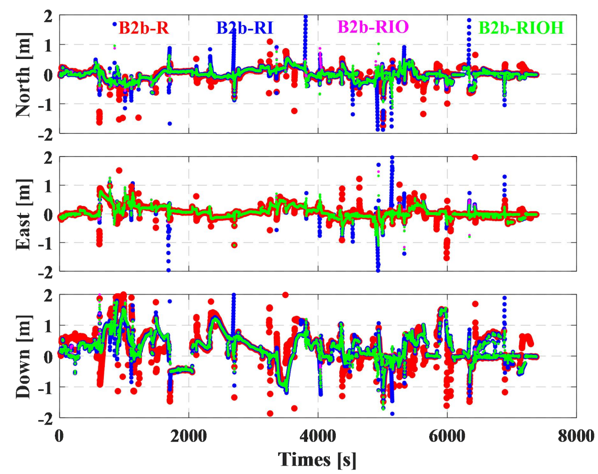

Fig. 6. Position differences of the BDS-3 B2b RTK (B2b-R), BDS-3 B2b RTK/INS (B2b-RI), BDS-3 B2b RTK/INS/Odometer (B2b-RIO), and BDS-3 B2b RTK/INS/Odometer/Heading (B2b-RIOH).

With the aid of INS, the positioning performances in terms of accuracy, stability, and continuity are greatly upgraded. Accordingly, the positioning performance of the BD3-B2b RTK/INS tight integration in the north, east, and down components are upgraded to 0.179 m, 0.192 m, and 0.524 m, with the improvements of 13.5%, 16.2%, and 12.3%, compared to the solutions of BDS-3 B2b RTK-only mode. Besides, it can see that the periods without RTK-only outputs also provide solutions in RTK/INS tight integration mode. However, due to the frequent complete signal outages in this test, the accuracy of RTK/INS tight integration mode during these periods will drift with time. Such position drifts could be weakened (i.e., 2640 s) after introducing the constraints of the odometer and NHC. Accordingly, the position RMSE values in the three directions are up to 0.174 m, 0.192 m, and 0.511 m, with about extra 2.8%, 0.0%, and 2.5% improvements. Here, we noticed that the position RMSE values of BDS3-B2b RTK/INS/Odometer/NHC tight integration are close to that of heading measurements-assisted BDS3-B2b RTK/INS/Odometer/NHC tight integration. This phenomenon may be due to the fact that heading observations mainly affected the accuracy of attitudes estimation, which can be concluded from Eq. (22). Such attitude influence is limited and only presents effects on the position from level-arm correction. For instance, only millimeter-level position enhancements appear in the north and vertical components.

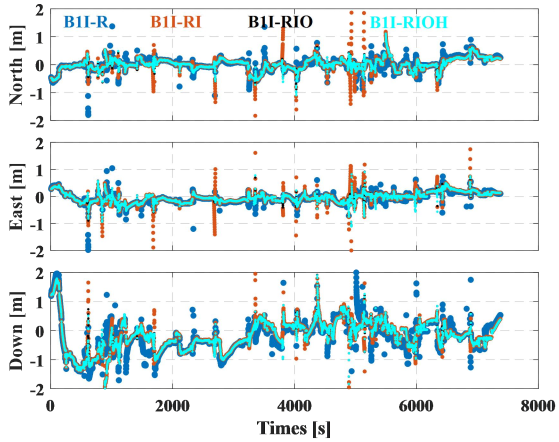

Fig. 7. Position differences of the BDS-3 B1I RTK (B1I-R), BDS-3 B1I RTK/INS (B1I-RI), BDS-3 B1I RTK/INS/Odometer (B1I-RIO), and BDS-3 B1I RTK/INS/Odometer (B1I-RIOH).

As a comparison, we also provided the position results of BDS-3 B1I in Fig. 7. According to the statistics, B2b solutions present a little higher accuracy in the north and vertical direction with the corresponding average improvements of 15.3% and 2.3%, and a little worse accuracy in the east component with about 10.7% decrements. Such differences may be related to the satellite observation quality. However, the accuracy in three-dimensional of the B1I-based solutions are close to these of the B2b-based solutions.

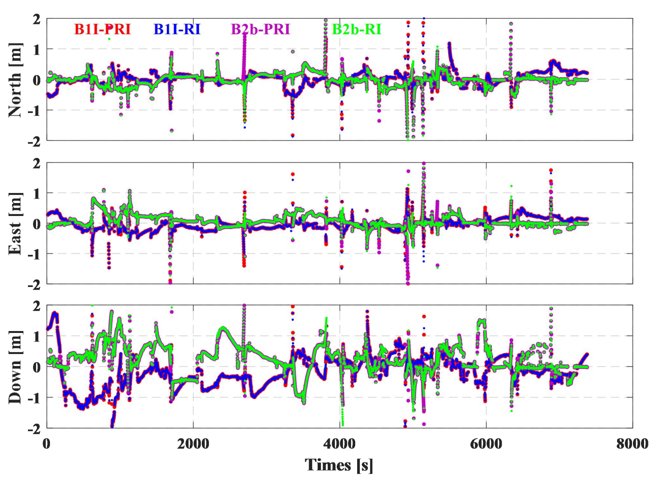

Fig. 8. Position differences of the BDS-3 B1I RTK/INS with Psi model (B1I-PRI), BDS-3 B1I RTK/INS with M-Psi model (B1I-RI), BDS-3 B2b RTK/INS with Psi model (B2b-PRI), BDS-3 B2b RTK/INS with M-Psi model (B2b-RI).

TABLE III

POSITION RMSE OF DIFFERENT SOLUTIONS

Schemes	North (m)	East (m)	Down (m)
B2b-R	0.207	0.229	0.683
B2b-RI	0.179	0.192	0.524
B2b-PRI	0.179	0.191	0.524
B2b-RIO	0.174	0.192	0.511
B2b-RIOH	0.173	0.192	0.509
B1I-R	0.246	0.187	0.627
B1I-RI	0.208	0.178	0.550
B1I-PRI	0.208	0.178	0.547
B1I-RIO	0.206	0.176	0.544
B1I-RIOH	0.206	0.175	0.544

Besides, we also investigated the effect of different state modes of multi-sensor integration system on its positioning accuracy. Fig. 8 shows the position differences of RTK/INS tight integration based on the Psi-angle model and the Modified Psi-angle model (M-Psi). According to the statics in Table III, the results based on the above two models are nearly identical. This is because the M-Psi model, a modified version of the Psi model, is mainly designed to solve the problem of the existence of the polluted specific force. During the test, the carrier cannot reach such high-speed motion in most epochs (as shown in Fig. 1). Therefore, the specific force has a meager impact on the state prediction.

According to the conclusions above, the BDS-3 positioning performance in terms of accuracy, reliability, and continuity could be gradually enhanced using the low-cost IMU, odometer, NHC, and heading measurements.

2) *Impacts on velocimetry*

Velocity and attitude are also the basic navigation parameters. Therefore, the differences in velocity are depicted in Figs. 9 and 10, and the corresponding RMSE are listed in Table IV. Accordingly, the velocity RMSE of BDS-3 B2b RTK/INS tight integration are 2.1 cm/s, 1.9 cm/s, and 3.1 cm/s in the three directions, with the enhancements of 50.0%, 38.7%, and 70.5% compared to the BDS-3 B2b RTK-only mode. After introducing the odometer measurements and NHC into RTK/INS tight integration, the velocity RMSE values are upgraded to 2.1 cm/s, 1.8 cm/s, and 2.3 cm/s, with another 0.0%, 5.3%, and 25.8% improvements in the north, east, and down directions. To some extent, such improvements in horizontal are not obvious. But it is visible in the vertical direction. This is due to the strength of satellite-user geo-structure being strong in horizontal and weak in vertical. While applying the odometer/NHC, the geo-structure in the vertical direction can be significantly improved. Therefore, high accuracy velocity in environments with good satellite tracking can be provided by using GNSS/INS tight integration, and the velocity accuracy in vertical can be visibly enhanced after introducing odometer/NHC [20]. While suffering satellite signal outages, the velocity observations can be strongly and directly observed by odometer/NHC (as shown in Eq. (14)), which would retain the accuracy of velocity. For example, the north velocity differences of scheme B2b-RI drift to about ±30 cm/s at epochs of 5090 s and 6290 s. But such drifts completely disappear while using the B2b-RIO mode. Similar to the position performance, the velocity results of B2b-RIOH are close to that of B2b-RIO. Besides, the velocity accuracy of BDS-3 B1I-based solutions is near to these B2b-based solutions, and the velocity based on the M-Psi-angle model are comparable to that of based on the Psi-angle model.

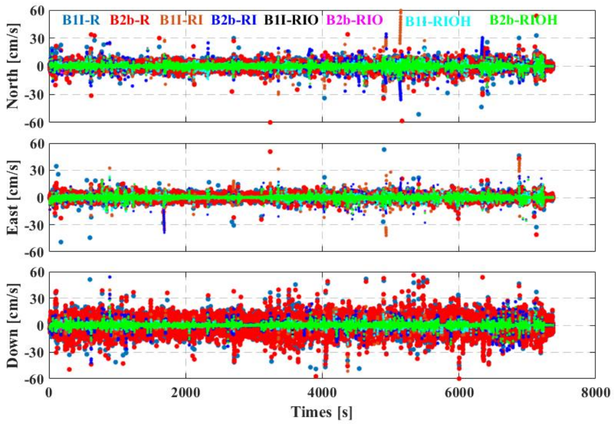

Fig. 9. Velocity differences of the BDS-3 B1I RTK (B1I-R), BDS-3 B2b RTK (B2b-R), BDS-3 B1I RTK/INS (B1I-RI), BDS-3 B2b RTK/INS (B2b-RI), BDS-3 B1I RTK/INS/Odometer (B1I-RIO), BDS-3 B2b RTK/INS/Odometer (B2b-RIO), BDS-3 B1I RTK/INS/Odometer (B1I-RIOH), BDS-3 B2b RTK/INS/Odometer/Heading (B2b-RIOH).

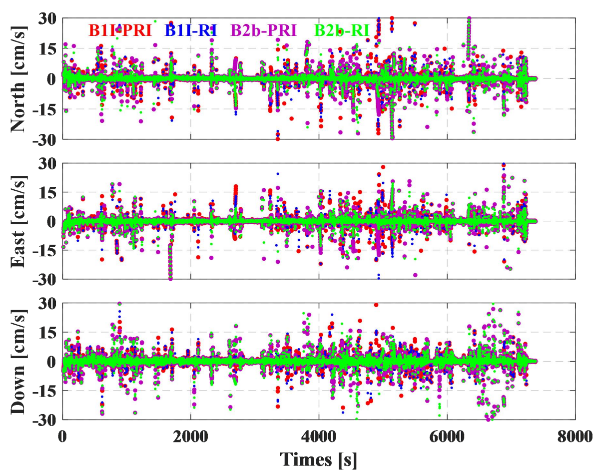

Fig. 10. Velocity differences of the BDS-3 B1I RTK/INS with Psi model (B1I-PRI), BDS-3 B1I RTK/INS with M-Psi model (B1I-RI), BDS-3 B2b RTK/INS with Psi model (B2b-PRI), BDS-3 B2b RTK/INS with M-Psi model (B2b-RI).

TABLE IV

VELOCITY RMSE OF DIFFERENT SOLUTIONS

Schemes	North (cm/s)	East (cm/s)	Down (cm/s)
B2b-R	4.2	3.1	10.5
B2b-RI	2.1	1.9	3.1
B2b-PRI	2.1	1.8	3.2
B2b-RIO	2.1	1.8	2.3
B2b-RIOH	2.1	1.8	2.3
B1I-R	5.1	3.4	10.0
B1I-RI	2.0	1.7	2.4
B1I-PRI	1.8	1.5	2.3
B1I-RIO	1.9	1.6	1.8
B1I-RIOH	1.9	1.6	1.8

3) Impacts on attitude determination

The differences in attitude are depicted in Figs. 11 and 12. According to the attitudes results in Table V, the accuracies of heading angles of RTK/INS tight integration are lower than these of roll and pitch due to the weak observability of the gyroscope in the vertical direction [24]. Fortunately, such observability can be significantly enhanced by using the odometer/NHC, and the heading angle can also be measured directly by dual-antenna heading measurements (as shown in Eqs. (16) and (22)). Accordingly, the attitude RMSE values of BDS-3 B2b RTK/INS/Odometer/NHC tight integration are 0.087°, 0.054°, and 0.122°, with enhancements of 16.9% and 62.9% in pitch and heading angles, compared to these of BDS-3 RTK/INS tight integration. After introducing the heading measurements provided by dual-antenna GNSS solutions, such heading improvements could be up to 73.9 %. Meanwhile, we noticed that the convergence time of yaw angle is visibly enhanced while using the odometer/NHC, the dual-antenna heading, or the two together. Similar to the results of position and velocity, the accuracies of BDS-3 B1I-based solutions are close to these of B2b-based solutions. While applying different state models, we noticed that the heading accuracy based on the Psi-angle model is litter higher than that of these based on the M-Psi-angle model, which presents about 10.3% and 13.8% while using the BDS-3 B2b and B2I observations, respectively. We noticed that the largest heading angle difference between the M-Psi and Psi model occurs at 4675 s. In such an epoch, the velocity in the horizontal direction reaches the maximum of 31.078 m/s (as shown in Fig. 2). Therefore, it can be concluded that the high-speed motion amplifies the effect of specific force terms on state estimates.

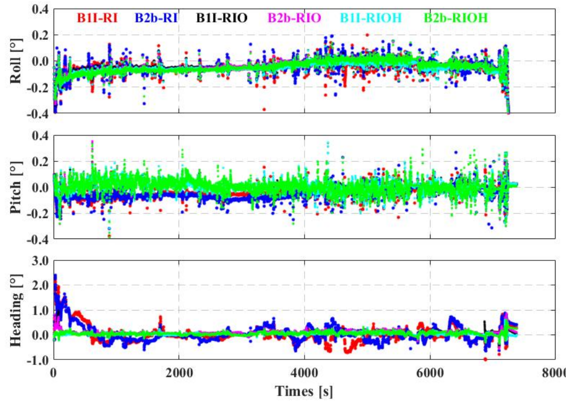

Fig. 11. Attitude differences of the BDS-3 B1I RTK (B1I-R), BDS-3 B2b RTK (B2b-R), BDS-3 B1I RTK/INS (B1I-RI), BDS-3 B2b RTK/INS (B2b-RI), BDS-3 B1I RTK/INS/Odometer (B1I-RIO), BDS-3 B2b RTK/INS/Odometer (B2b-RIO), BDS-3 B1I RTK/INS/Odometer (B1I-RIOH), BDS-3 B2b RTK/INS/Odometer/Heading (B2b-RIOH).

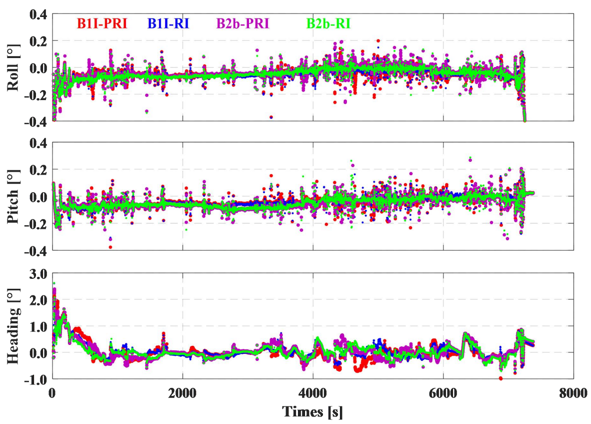

Fig. 12. Attitude differences of the BDS-3 B1I RTK/INS with Psi model (B1I-PRI), BDS-3 B1I RTK/INS with M-Psi model (B1I-RI), BDS-3 B2b RTK/INS with Psi model (B2b-PRI), BDS-3 B2b RTK/INS with M-Psi model (B2b-RI).

TABLE V
ATTITUDE RMSE OF DIFFERENT SOLUTIONS

Schemes	Roll (°)	Pitch (°)	Heading (°)
B2b-RI	0.086	0.065	0.329
B2b-PRI	0.087	0.064	0.295
B2b-RIO	0.087	0.054	0.122
B2b-RIOH	0.090	0.054	0.086
B1I-RI	0.089	0.057	0.340
B1I-PRI	0.089	0.059	0.293
B1I-RIO	0.088	0.050	0.124
B1I-RIOH	0.092	0.050	0.068

C. Improvements in single-frequency DD ambiguity resolution

As described in the Methodology part, ADOP, to a great extent, is an approximate description of the average accuracy of the DD float ambiguity. This section will present the impacts of the presented method on single-frequency DD ambiguity resolution.

1) Impacts on ADOP

According to [42], the ambiguity success-rate can be larger than 0.999 while the ADOP is smaller than 0.12. Figs. 13 and 14 showed the time series of ADOP values calculated by different modes based on BDS-3 B2b and B1I SF observations, respectively. The corresponding RMS are listed in Tables VI and VII. Accordingly, the ADOP RMS values based on B2b are 0.594, 0.0356, 0.0352, 0.0263, and 0.0262 for the schemes R, RI, PRI, RIO, and RIOH. Similarly, the corresponding ADOP RMS values for B1I-based schemes are 0.590, 0.0585, 0.0582, 0.0435, and 0.0432. Visibly, the above results are consistent with the theoretical part in Subsection "*Multi-sensor augmented ambiguity resolution*". By integrating with extra sensors, the ambiguity accuracy in terms of ADOP would be improved to varying degrees. Such phenomenon is mainly due to the different accuracy of position and attitude in different integration modes. For example, the scheme RIOH provides the greatest improvement in position and attitude accuracy (the smallest RMSE of position and attitude). Therefore, the corresponding ADOP is the lowest one among all schemes. Generally, the presented model could improve ambiguity accuracy and compress the ambiguity search space.

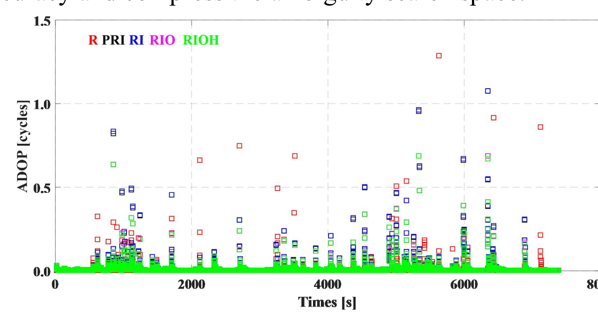

Fig. 13. Time series of ADOP value of BDS-3 B2b solutions.

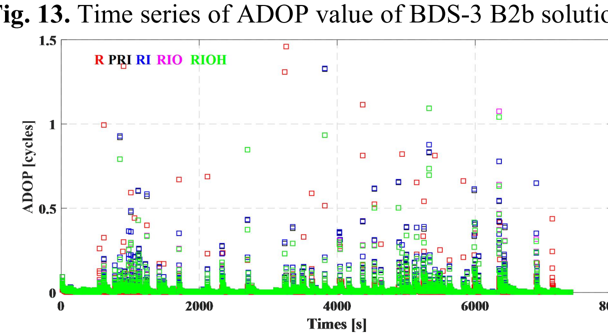

Fig. 14. Time series of ADOP value of BDS-3 B1I solutions.

2) Impacts on reliability of ambiguity resolution

Usually, the position error should be closed to zero while DD ambiguities are fixed accurately. However, such a character would not be satisfied by the biased ambiguities. According to

This article has been accepted for publication in IEEE Internet of Things Journal. This is the author's version which has not been fully edited and content may change prior to final publication. Citation information: DOI 10.1109/JIOT.2022.3227019

[24], the biased ambiguity would lead to a jump in terms of position error. Figs. 15 and 16 show the differences in position errors based on B2b and B1I in the adjacent epoch under the ambiguity fixed condition. It can be seen that most of the jump phenomenon in RTK disappeared after adding INS augmentation, and such disappearance are more obvious after furtherly introducing the enhancements of odometer/NHC and heading measurements. This is because the integration of IMU data, odometer data, and heading measurements could restrain the white noise-depended variations of the float solution (as listed in Tables VI and VII) and improve the ambiguity accuracy (as described in ADOP). It contributes to reduce the probability of generating a biased ambiguity.

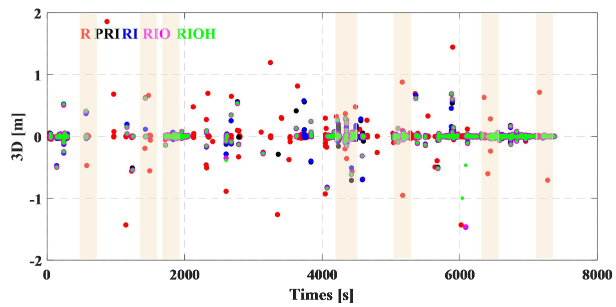

Fig. 15. The differences of position errors in the adjacent epoch of the BDS-3 B2b modes of R, PRI, RI, RIO, and RIOH under the ambiguity fixed condition.

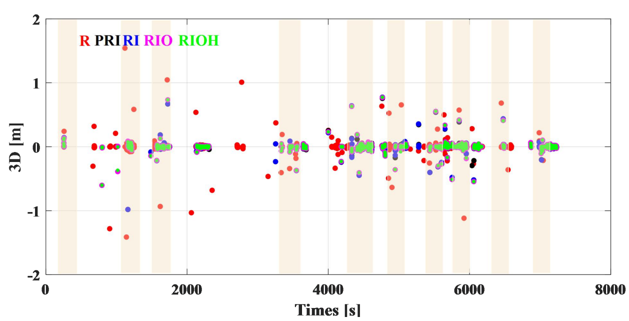

Fig. 16. The differences of position errors in the adjacent epoch of the BDS-3 B1I modes of R, PRI, RI, RIO, and RIOH under the ambiguity fixed condition.

Under the condition of float ambiguity, the position RMSE values of BDS-3 B2b RTK/INS tight integration are 0.305 m and 0.573 m, with the enhancements of 13.6% and 21.9% in horizontal and vertical directions, compared to the solutions of RTK-only. After the fusion of odometer/NHC data, such percentages are up to 14.2% and 23.4%. After furtherly adding the heading measurements, the corresponding improvements are slighter up to 14.6% and 23.4%. Similar enhancements can also be found in the B1I-based solutions. Under the condition of fixing ambiguity, the position errors under the conditions of the Biased Fixed (BF) ambiguity and the Un-Biased Fixed (UBF) ambiguity of different modes in horizontal and vertical components are shown in Figs. 17 and 18. The corresponding RMSE are listed in Tables VI and VII. Accordingly, the ambiguity fixed rate of BDS-3 B2b are 29.8%, 31.0%, 31.1%, 30.5%, and 30.7% for schemes of R, RI, PRI, RIO, and RIOH, and the corresponding fixed rate of BDS-3 B1I are 16.3%, 17.9%, 17.5%, 18.2%, and 18.3%. Besides, the BF rate is gradually decreased with the enhancements of multi-sensors. According to the statistics, the BF rate of BDS-3 B2b RIOH is 5.9%, with reductions of 10.8%, 1.9%, 2.0%, and 0.01% compared to the other four modes, and that of BDS-3 B1I RIOH is 4.7% with reductions of 4.7%, 0.4%, 0.5 %, and 0.02%. The position RMSE values of BDS-3 B2b RTK/INS tight integration in horizontal and vertical components are 0.232 m and 1.163 m, with enhancements of 22.8% and 9.9% compared to the solutions of BDS-3 B2b RTK-only. The percentages in horizontal are up to 45.3% after applying the odometer/NHC/heading measurements augmentation. Similar improvements can also be found in the B1I-based solutions. It is reasonable to conclude that the presented model could smooth the position solutions and reduce the probability of large errors. For the solutions of UBF ambiguity, the position accuracies of BDS-3 B2b on average are 0.111 m and 0.240 m in horizontal and vertical directions, which is higher than that of BD3 B1I (0.227 m and 0.374 m). Besides, we noticed that the different state models hardly influence the positioning accuracy of BF or UBF. But the solutions based on the M-Psi-angle model provide better results in terms of fixed rate and UBF rate.

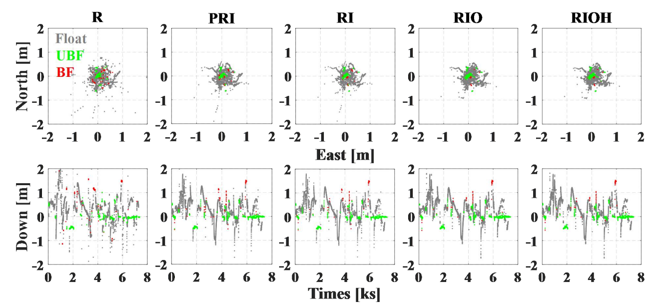

Fig. 17. Position errors under the conditions of float/biased fixed ambiguity (BF) /unbiased fixed ambiguity (UBF) ambiguity of the BDS-3 B2b modes of R, PRI, RI, RIO, and RIOH in horizontal and vertical directions.

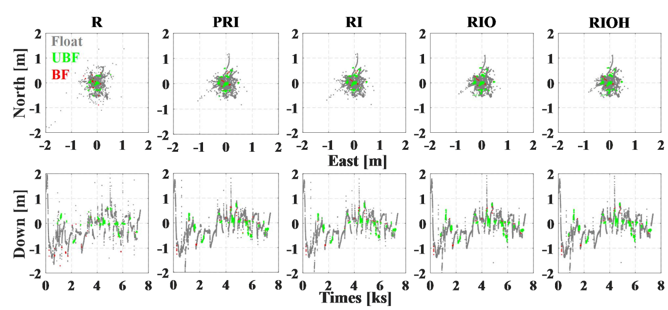

Fig. 18. Position errors under the conditions of float/biased fixed ambiguity (BF) /unbiased fixed ambiguity (UBF) of the BDS-3 B1I modes of R, PRI, RI, RIO, and RIOH in horizontal and vertical directions.

TABLE VI

POSITION RMSE OF THE BDS-3 B2B MODES OF R, RI, PRI, RIO, AND RIOH UNDER THE CONDITIONS OF FLOAT/BIASED FIXED AMBIGUITY (BF) /UNBIASED FIXED AMBIGUITY (UBF).

Schemes	B2b	R	PRI/RI	RIO	RIOH
Float (m)	Horizontal	0.353	0.304/0.305	0.303	0.302
	Vertical	0.734	0.576/0.573	0.562	0.562
UBF(m)	Horizontal	0.118	0.111/0.112	0.108	0.107
	Vertical	0.280	0.230/0.232	0.230	0.229
BF(m)	Horizontal	0.300	0.206/0.232	0.164	0.164
	Vertical	1.181	1.126/1.163	1.204	1.200
ADOP		0.0594	0.0352/0.0356	0.0263	0.0262
Fixed-rate		29.82%	31.03%/31.11%	30.46%	30.74%
BF-rate		16.70%	7.92%/7.86%	5.94%	5.93%

TABLE VII

POSITION RMSE OF THE BDS-3 B1I MODES OF R, RI, PRI, RIO, AND RIOH UNDER THE CONDITIONS OF FLOAT/BIASED FIXED AMBIGUITY (BF) /UNBIASED FIXED AMBIGUITY (UBF).

Schemes	B1I	R	PRI/RI	RIO	RIOH
Float (m)	Horizontal	0.324	0.281/0.282	0.279	0.278
	Vertical	0.656	0.572/0.576	0.572	0.573
UBF(m)	Horizontal	0.203	0.234/0.233	0.233	0.232
	Vertical	0.357	0.383/0.381	0.374	0.375
BF(m)	Horizontal	0.282	0.247/0.250	0.248	0.248
	Vertical	0.954	0.706/0.706	0.719	0.719
ADOP		0.0590	0.0582/0.0585	0.0435	0.0432
Fixed-rate		16.27%	17.52%/17.68%	18.23%	18.31%
BF-rate		9.39%	5.18%/5.13%	4.74%	4.72%

IV. CONCLUSIONS

To extend the potential application area of BDS-3 single-frequency RTK and improve the navigation performance of vehicle-borne under complex urban environments, we present a multi-sensor and analytical observations tightly augmented the single-frequency RTK model based on a modified Psi-angle state model and BDS-3 new signal B2b. In such a model, the BDS-3 B2b observations are tightly integrated with low-cost MEMS IMU data, odometer measurements, dual-antenna attitude, and non-holonomic constraint. After describing the corresponding mathematical models in detail, a set of vehicle-borne data collected along the fifth ring road of Beijing was processed and analyzed to present the comprehensive performance of the presented model in terms of positioning, velocimetry, attitude determination, and ambiguity credible fixing rate. According to the results, the position RMSE of RTK/INS tight integration could bring about 13.5%, 16.2%, and 12.3% enhancements, compared to these of the BDS-3 B2b RTK-only mode. While using the odometer/NHC/dual-antenna attitude aided RTK/INS/ tight integration, the position accuracy would be further enhanced. Such conclusions could also be found in the solutions of velocity and attitude. However, the attitude enhancements are mainly in the heading angle due to the observability improvements of the gyroscope in the vertical direction and the direct observability of the heading angle. Besides, the performance of ambiguity resolution could also be improved while using the presented model, which mainly benefits from the enhancements in position and attitude. similarly, it also emerged that the solutions of the M-Psi-angle model achieved better results in terms of unbiased fixed ambiguity rate.

REFERENCES

[1] N. El-Sheimy, Y. Li, "Indoor Navigation: State of Art and Future Trends," Satellite Navigation, vol. 2, no. 1, pp. 7, 2021.

[2] B. Li, Z. Zhang, N. Zang, S. Wang, "High-precision GNSS ocean positioning with BeiDou short-message communication," Journal of Geodesy, vol. 93, no. 4, pp. 125–139, 2018.

[3] Y. Yao, C. Liu, C. Xu, "A New GNSS-Derived Water Vapor Tomography Method Based on Optimized Voxel for Large GNSS Network," Remote Sensing, vol. 12, no. 14, pp. 2306, 2020.

[4] K. Zhang, Y. Wang, W. Gan, S. Liang, "Impacts of Local Effects and Surface Loads on the Common Mode Error Filtering in Continuous GPS Measurements in the Northwest of Yunnan Province, China," Sensors, vol. 20, no. 18, pp. 5408, 2020.

[5] P. Shen, F. Cheng, X. Lu, X. Xiao, Y. Ge, "An Investigation of Precise Orbit and Clock Products for BDS-3 from Different Analysis Centers," Sensors, vol. 21, no. 5, pp. 1596, 2021.

[6] Y. Yang, Y. Xu, J. Li, C. Yang, "Progress and performance evaluation of BeiDou global navigation satellite system: Data analysis based on BDS-3 demonstration system," Science China Earth Sciences, vol. 61, no. 5, pp. 614-624, 2018.

[7] Y. Yang, Y. Mao, B. Sun, "Basic performance and future developments of BeiDou global navigation satellite system," Satellite Navigation, vol. 1, no. 1, pp. 1, 2020.

[8] CSNO "BeiDou Navigation Satellite System Open Service Performance Standard (Version3.0)," 2021.

[9] Q. Zhao, B. Sun, Z. Dai, Z. Hu, C. Shi, J. Liu, "Real-time detection and repair of cycle slips in triple-frequency GNSS measurements," GPS Solutions, vol. 19, no. 3, pp. 381-391, 2015.

[10] D. Psychas, S. Verhagen, P. J. G. Teunissen, "Precision analysis of partial ambiguity resolution-enabled PPP using multi-GNSS and multi-frequency signals," Advances in Space Research, vol. 66, no. 9, pp. 2075-2093, 2020.

[11] X. Li, X. Li, G. Liu, G. Feng, Y. Yuan, K. Zhang, X. Ren, "Triple-frequency PPP ambiguity resolution with multi-constellation GNSS: BDS and Galileo," Journal of Geodesy, vol. 93, no. 8, pp. 1105–1122, 2019.

[12] S. Gu, C. Shi, Y. Lou, J. Liu, "Ionospheric effects in uncalibrated phase delay estimation and ambiguity-fixed PPP based on raw observable model," Journal of Geodesy, vol. 89, no. 5, pp. 447-457, 2015.

[13] Y. Yang, J. Li, A. Wang, J. Xu, H. He, H. Guo, J. Shen, X. Dai, "Preliminary assessment of the navigation and positioning performance of BeiDou regional navigation satellite system," Science China Earth Sciences, vol. 57, no. 1, pp. 144-152, 2013.

[14] G. Wang, K. Jong, Q. Zhao, Z. Hu, J. Guo, "Multipath analysis of code measurements for BeiDou geostationary satellites," GPS Solutions, vol. 19, no. 1, pp. 129-139, 2014.

[15] Z. Zhang, B. Li, L. Nie, C. Wei, J. Song, S. Jiang, "Initial assessment of BeiDou-3 global navigation satellite system: signal quality, RTK and PPP," GPS Solutions, vol. 23, no. 4, pp. 111, 2019.

[16] C. Shi, X. Wu, F. Zheng, X. Wang, J. Wang, "Modeling of BDS-2/BDS-3 single-frequency PPP with B1I and B1C signals and positioning performance analysis," Measurement, vol. 178, no. 1, pp. 109355, 2021.

[17] Y. Yuan, X. Mi, B. Zhang, "Initial assessment of single- and dual-frequency BDS-3 RTK positioning," Satellite Navigation, vol. 1, no. 31, pp. 1-7, 2020.

[18] Y. Liu, Z. Gao, Q. Xu, Y. Li, L. Chen, "Assessing partial ambiguity resolution and WZTD-constraint multi-frequency RTK in an urban environment using new BDS signals," GPS Solutions, vol. 26, no. 88, 2022. https://doi.org/10.1007/s10291-022-01274-8.

[19] D. B. Cox "Integration of GPS with inertial navigation systems," Navigation, vol. 25, no. 2, pp. 236–245, 1978.

[20] Z. Gao, "Research on the methodology and application of the integration between the multi-constellation GNSS PPP and inertial navigation system," Ph.D. dissertation, University of Wuhan, Wuhan, China, 2016.

[21] X. Li, X. Li, J. Huang, Z. Shen, B. Wang, Y. Yuan, K. Zhang, "Improving PPP–RTK in urban environment by tightly coupled integration of GNSS and INS," Journal of Geodesy, vol. 95, no. 12, pp. 132, 2021.

[22]H. Han, J. Wang, J. Wang, X. Tan, "Performance Analysis on Carrier Phase-Based Tightly-Coupled GPS/BDS/INS Integration in GNSS Degraded and Denied Environments," Sensors, vol. 15, no. 4, pp. 8685-8711, 2015.

[23]S. Zhao, Y. Chen, J. Farrell, "High Precision Vehicle Navigation in Urban Environments using a MEM's IMU and Single-frequency GPS Receiver," IEEE Transactions on Intelligent Transportation Systems, vol. 17, no. 10, pp. 2854-2867, 2016.

[24]T. Li, "Research on the Tightly Coupled Single-frequency multi-GNSS/INS/Vision Integration for Precise Position and Orientation Estimation," Ph.D. dissertation, University of Wuhan, Wuhan, China, 2019.

[25]P. Yan, J. Jiang, Y. Tang, F. Zhang, D. Xie, J. Wu, J. Liu, J. Liu, "Dynamic Adaptive Low Power Adjustment Scheme for Single-Frequency GNSS/MEMS-IMU/Odometer Integrated Navigation in the Complex Urban Environment," Remote Sensing, vol. 13, no. 16, pp. 3236, 2021.

[26]T. Li, H. Zhang, Z. Gao, X. Niu, N. El-Sheimy, "Tight Fusion of a Monocular Camera, MEMS-IMU, and Single-Frequency Multi-GNSS RTK for Precise Navigation in GNSS-Challenged Environments," Remote Sensing, vol. 11, no. 6, pp. 610, 2019.

[27]C. Qian, H. Liu, J. Tang, Y. Chen, H. Kaartinen, A. Kukko, L. Zhu, X. Liang, L. Chen, J. Hyyppa, "An integrated GNSS/INS/LiDAR-SLAM positioning method for highly accurate forest stem mapping," Remote sensing, vol. 9, no. 1, pp. 3, 2016.

[28]G. Dissanayake, S. Sukkarieh, E. Nebot, H. Durrant-Whyte, "The aiding of a low-cost strapdown inertial measurement unit using vehicle model constraints for land vehicle applications," IEEE Transactions on Robotics & Automation, vol. 17, no. 5, pp. 731-747, 2001.

[29]X. Niu, Y. Li, Q. Zhang, Y. Cheng, C. Shi, "Observability Analysis of Non-Holonomic Constraints for Land-Vehicle Navigation Systems," Journal of Global Positioning Systems, vol. 11, no. 1, pp. 80-88, 2012.

[30]Z. Niu, P. Nie, L. Tao, J. Sun, B. Zhu, "RTK with the Assistance of an IMU-Based Pedestrian Navigation Algorithm for Smartphones," Sensors, vol. 19, no. 14, pp. 3228, 2019.

[31]E. H. Shin, "Estimation techniques for low-cost inertial navigation," University of Calgary, Calgary, Canada, 2005.

[32] B. M. Scherzinger, D. B. Reid, "Modified Strapdown Inertial Navigator Error Models," In: Proceedings of the IEEE Symposium on Position Location and Navigation (PLANS), 1994.

[33]Z. Gao, M. Ge, Y. Li, Y. Pan, Q. Chen, H. Zhang, "Modeling of multi-sensor tightly aided BDS triple-frequency precise point positioning and initial assessments," Information Fusion, vol. 55, no. C, pp. 184-198, 2020.

[34]Z. Gao, M. Ge, Y. Li, Q. Chen, Q. Zhang, X. Niu, H. Zhang, W. Shen, H. Schuh, "Odometer, low-cost inertial sensors, and four-GNSS data to enhance PPP and attitude determination," GPS Solutions, vol. 22, no. 3, pp. 22-57, 2018.

[35]Y. Shu, "Algorithms and Applications of Multi-Antenna GNSS/INS Tightly-Coupled Integration for Attitude Determination," Ph.D. dissertation, University of Wuhan, Wuhan, China, 2018.

[36]S. Carcanague, "Low-cost GPS/GLONASS Precise Positioning Algorithm in Constrained Environment," Ph.D. dissertation, Institute National Polytechnique de Toulouse-INP, Toulouse, France, 2014.

[37]X. Zhang, F. Zhu, Y. Zhang, F. Mohamed, W. Zhou, "The improvement in integer ambiguity resolution with INS aiding for kinematic precise point positioning" Journal of Geodesy, vol. 93, no. 3, pp. 993-1010, 2018.

[38]Crassidis JL, Junkins JL, "Optimal estimation of dynamics systems," CRC Press, Boca Raton, pp 145–146, 2011.

[39]P. J. G. Teunissen, D. Odijk, "Ambiguity dilution of precision: Definition, properties and application," In: Proceedings of the ION GPS, pp. 891–899, 1997.

[40]T. Takasu, A. Yasuda, "Kalman-filter-based integer ambiguity resolution strategy for long-baseline RTK with ionosphere and troposphere estimation," In: Proceedings of the ION GNSS, pp. 161-171, 2010.

[41]P. J. G. Teunissen, "The Least-Squares Ambiguity Decorrelation Adjustment: A Method for Fast GPS IntegerAmbiguity Estimation," Journal of Geodesy, vol. 70, pp. 65–82, 1995.

[42]P. J. G. Teunissen, R. Odolinski, D. Odijk, "Instantaneous BeiDou+GPS RTK positioning with high cut-off elevation angles," Journal of Geodesy, vol. 88, no. 4, pp. 335-350, 2013.

Qiaozhuang Xu, is currently a Ph.D. candidate at the China University of Geosciences Beijing. His research interests are multi-GNSS real-time kinematic positioning theories, GNSS/INS integration, and multi-sensor fusion methods.

Zhouzheng Gao, is an Associate Professor and doctoral supervisor at the China University of Geosciences Beijing, and received his Ph.D. degree from the School of Geodesy and Geomatics, Wuhan University, in 2016. His research interests include GNSS seismology, GNSS precise positioning algorithms, precise indoor positioning and navigation, and the integration between GNSS and multi-sensor.

Jie Lv, is currently a Ph.D. candidate at the China University of Geosciences Beijing. Her research interests are GNSS precise positioning algorithms and multi-sensors fusion methods.

Cheng Yang, is an Associate Professor and doctoral supervisor at the China University of Geosciences Beijing, and received his Ph.D. degree from the department of Land Survey and Geo-Informatics, The Hong Kong Polytechnic University, in 2017. His research interests include GNSS positioning algorithms, indoor positioning and navigation, and multi-sensor integrations.